Corrosion of 304 stainless, Inconel 625, and Haynes 230 in a Chloride Salt-Based Thermal Storage Medium

Wenhua Yu, Dileep Singh, and David M. France
Applied Materials Division, Argonne National Laboratory
9700 South Cass Avenue, Lemont, IL 60439, USA
Contact e-mail: wyu@anl.gov (W. Yu), dsingh@anl.gov (D. Singh), dfrance@uic.edu (D.M. France)

One of the critical challenges for latent-heat thermal energy storage systems in concentrating solar power applications is corrosion of metallic alloys as containment and heat transfer fluid tube materials in corrosive salts at high temperatures. In this study, the effects of $MgCl_2$ on the corrosion of stainless steel 304, Inconel 625, and Haynes 230 alloys were investigated through embedded metal samples in the graphite foam/$MgCl_2$ storage medium. Four experimental testing modules were fabricated and experimental tests were conducted under controlled environment by heating the testing modules to and keeping them at 750 °C for 100 h, 200 h, 500 h, and 1000 h. The estimated corrosion rates based on the weight losses for stainless steel 304, Inconel 625, and Haynes 230 were 94 µm/year, 9 µm/year, and 8 µm/year, respectively. The fitted equations for the loss of the thickness as functions of the exposure time show that the corrosion rates decrease with the exposure time. The results on the corrosion zones or depths and chromium segregation ranges of the experimental samples are also presented.

Keywords Corrosion, alloy, $MgCl_2$, high temperature

1. Introduction

Concentrating solar power (CSP) has an inherently transient nature due to its unavailability during nighttime and cloudy days, which adversely affects the load leveling for grid electricity supply, the overall efficiency of the CSP electric plant, and the levelized cost of electricity. With this limitation in mind, thermal energy storage (TES) has been developed to improve operations of CSP electric plants. Currently, implemented TES systems in existing CSP electric plants are generally based on sensible heat storage (Ref 1-5), which has some disadvantages including complex pumping systems, large storage mass volumes, high-degree insulations, and low solar-to-electric efficiencies (Ref 6). Latent heat-based TES systems developed recently have two very important advantages compared to sensible heat-based TES systems: a much smaller storage system size due to the vast amount of energy from the latent heat of fusion of a phase-change material (PCM) and a very narrower operation temperature range related to the melting/solidification temperature of the PCM, both of which lead to high system efficiencies (Ref 7). Among various PCM salts, chloride salts and their eutectic or non-eutectic mixtures have been identified as candidates for PCMs in TES systems of high-temperature CSP plants (such as supercritical carbon dioxide Brayton cycles) due to their appropriate melting/solidification temperatures, high latent heats of fusion, high thermal stability limits, and low prices (Ref 8-10).

One of the challenges for latent heat-based TES systems in CSP applications is the very low thermal conductivities of applicable PCMs (Ref 11). As a consequence, the heat transfer rate between the PCM and the charging/discharging heat transfer fluid (HTF) is also very low, resulting in the requirement of a significantly large number of HTF tubes for charging and discharging a TES system. Various technologies have been proposed to enhance the heat transfer on both sides of the PCM and the HTF, including finned HTF tubes (Ref 12-14), heat pipes (Ref 15, 16), dispersed high-thermal conductivity particles (Ref 17), metal foam structures (Ref 18-21), graphite foam structures (Ref 22-27), or their combinations (Ref 28). Another challenge for latent heat-based TES systems in CSP applications is corrosion of metallic alloys as containment and HTF tube materials in chloride salts at high temperatures (Ref 6, 9, 10, 29-32). Corrosion of metallic alloys in molten chloride salts relates to multiple aspects of the interactions of chloride melts with covering gases and metallic alloys and the reactions in chloride melts (Ref 10). Excessive corrosion of metallic alloys can be caused by impurities in chloride salts in the form of moisture and oxygen (Ref 27, 30).

Previously, a shell-and-tube type TES system was developed by the present authors. The design of the latent heat-based TES system used high-porosity (>85%) graphite foam infiltrated with a PCM ($MgCl_2$) as a storage medium for enhanced thermal performance (Ref 22-27). The performance testing of laboratory-scale prototypes verified that the numerical predictions agreed well with the experimental data (Ref 26, 27). Behaviors and mechanisms of metal alloy corrosion related to chloride salts have been widely studied (Ref 6, 10, 30-32). Some general corrosion trends of various metal alloys have been established. However, corrosion is very sensitive to application conditions, and metal alloy corrosion behaviors specifically for the graphite foam/PCM ($MgCl_2$) thermal energy storage medium have not been studied. Therefore, there is a need for quantitative investigation under this application condition. The present study, through quantitative corrosion rate/depth measurements of three alloys from chloride salt PCM ($MgCl_2$), aimed (a) to establish corrosion behavior of metallic alloys in the realistic system environment of the proposed storage technology where the PCM was contained in the graphite foam pores and had limited contact with the alloys; (b) to evaluate the corrosion mitigation approaches of argon degassing/cleaning of PCM salt prior to and post infiltration; and therefore (c) to further validate the proposed storage technology.

2. Metal Alloy Samples and Corrosion Test Modules

Various alloys were surveyed based on the criteria of the yield stress, corrosion resistance, oxidation resistance, allowable stresses at elevated temperatures, current availability, etc. A literature search showed that several metal alloys, such as Haynes 230, Inconel 740H, Inconel 625, Inconel 617, ranked at the top for minimizing corrosion with chloride salts. However, upon discussions with the alloy vendors it was found that Inconel 625 was the only metal alloy among them currently available in the dimensions that would be suitable for the HTF tube material in latent heat-based TES systems. In this study, Haynes 230 and Inconel 625 were selected for corrosion testing. In addition, the effects of the PCM on an inexpensive containment material, stainless steel 304 (SS 304), was included. The chemical compositions of these three metal alloys used in this study are listed in Table 1 (Ref 33-35).

Table 1 Chemical composition of three metal alloys (mass %)

By using electrical discharge machining, corrosion test samples from three alloys were machined into cylinder shapes with dimensions of Φ3 mm × 4.76 mm for SS 304, Φ3 mm × 3 mm for Inconel 625, and Φ3 mm × 4 mm for Haynes 230. These test samples were embedded in graphite foam at two different depths, one close to its bottom and another near its top. The purpose of this arrangement was to investigate any potential differences in the moisture/oxygen pick-up by the PCM post infiltration. Six samples of each alloy were placed at the two depths as shown in Fig. 1a, with three samples of each alloy for each depth.

Fig. 1 Corrosion test modules and alloy test samples

The overall design of the corrosion test module is also shown in Fig. 1 where the container cylinders, bottom plates, top plates, and graphite foam disks were machined according to the design. The module accommodated three graphite foam disks shown in Fig. 1b. The middle and bottom disks were machined with nine recesses in each for housing the metal alloy samples. After machining, the container bottom plates were welded to the container cylinders, followed by a brazing process to ensure the graphite foam disks and the metal alloy samples remained in place during the $MgCl_2$ infiltration process.

3. $MgCl_2$ Infiltration

Prior to corrosion testing, the effectiveness of the infiltration process of the PCM ($MgCl_2$) into the graphite foam disks was investigated. The purpose of this investigation was to ensure (a) the complete infiltration of the PCM in the graphite foam and (b) the complete fill of the PCM around the embedded metal samples, which is important prior to corrosion testing on high-temperature alloys. For this investigation, special modules (test containers), shown in Fig. 1c, were fabricated.

The test containers were made of SS 304, and held three special graphite foam disks. The bottom two disks were each machined to house a single metal alloy sample. Prior to infiltration with PCM, alloy samples were placed in the graphite foam disks, and the disks were brazed to the wall of the test container to ensure the graphite foam disks and the metal samples remained in place during the infiltration process. Several trial runs of infiltration were conducted. Each infiltration test container was weighed before and after infiltration to verify the amount of salt infiltrated into the graphite foam. For an infiltration run, typical steps include evacuating and refilling with argon, heating and re-evacuating, and pressurizing and cooling. Post infiltration, each of the containers was cut open to examine the graphite foam and embedded metal samples.

As an example, Figure 1d shows the cut-open views of an infiltrated container. As shown in Fig. 1d, the graphite foam was well infiltrated overall and around the embedded metal sample. Figure 1d (ii) is the bottom of the container showing the PCM almost completely infiltrated. Figure 1d (iii) shows a metal alloy sample in the graphite foam. The PCM completely infiltrated the graphite foam around the metal alloy. These results established the good degree of infiltration of PCM both in the foam and around a metal sample, which was important for viable corrosion testing.

Four corrosion test modules were infiltrated with $MgCl_2$ by using the above procedure. After the infiltration, the top plates of the containers were welded closed in a vacuum environment. In addition, there was a vacuum port on the top plate of each container to remove any residual moisture/oxygen in the module. The completed corrosion test modules are shown in Fig. 1e.

4. Corrosion Experiments

4.1 Moisture and Oxygen Removal

For each of the corrosion test modules, a systematic moisture/oxygen removal process was followed. This included heating and holding the container at >600 °C, periodically evacuating the container under vacuum, and flushing the container with high purity argon gas. Figure 2 shows a typical profile obtained during this procedure. The first part of Fig. 2 is a detailed view of a portion of the second part. Note in the first part of Fig. 2 that there were two regimes, around 2 h and 200 °C and 6 h and 450 °C, where the inside pressure rose rapidly, indicative of emissions from minor decomposition of $MgCl_2$ and HCl gas release, respectively (Ref 36). After the corrosion test module vacuum pressure was stabilized for 96 h at 600 °C, the vacuum port was welded shut. This final welding was done under vacuum conditions to avoid any moisture or oxygen pick-up.

Fig. 2 Temperature and pressure profiles during moisture removal process

4.2 Corrosion Testing

Prior to corrosion testing, an Inconel 625 cap was welded to each of the test corrosion test modules as a backup to the vacuum port weld because the weld had a small thickness. This backup was particularly important for the long-term tests. Figure 1f shows the corrosion test modules after installation of the cap and prior to the start of the corrosion testing. Corrosion tests were conducted at 750 °C for 100 h, 200 h, 500 h, and 1000 h. Initially, all four corrosion test modules were placed in the furnace. After each test interval, the furnace was cooled down to retrieve a single corrosion test module, and then it was heated up again to continue testing. Consequently, all metal alloy samples in the first module removed from the furnace were subjected to 100 h. The metal alloys in the second module removed from the furnace were subjected to 200 h, etc.

4.3 Sample Cleaning

Post corrosion testing, corrosion test modules were cut open, and alloy samples were extracted. Figure 1g shows the embedded samples after the removal of graphite foam and salt around them. Because the salt and graphite foam were fused to the sample surfaces, the following cleaning procedure was followed: The alloy samples were sonicated for 15 minutes in an isopropanol bath, wiped to remove any residual $MgCl_2$/graphite foam, re-sonicated for 10 minutes in an isopropanol bath, dried in air and sonicated again for 5 minutes in an isopropanol bath, followed by air drying and furnace drying at 60–70 °C for 20 minutes.

5. Experimental Results and Discussion

Several methods can be used to determine corrosion rates of alloys in molten salts, including (a) weight and dimension changes with the exposure time, (b) corrosion zone/depth changes with the exposure time using microscopy, and (c) electrochemical techniques. In the present study, the first two approaches were used for monitoring corrosion of the alloys.

5.1 Corrosion Rate Measurements Based on Weight Losses

After the retrieved alloy samples were cleaned, their masses and dimensions were measured, and the results were compared to the original values. Figure 3 shows the weight losses for the three sets of alloys tested for 100 h, 200 h, 500 h, and 1000 h. For each of the alloys, samples placed in the upper and lower tiers of the container were combined to give an average value. Results reported were averages for 4-6 samples. The weight losses were high for the initial 100-h test for all the alloys. The weight losses for the 200-h and 500-h tests were of similar magnitudes. Further, for Inconel 625 and Haynes 230, the weight losses for the 1000-h test appeared to be smaller, but were within the scatter in the experimental data.

Fig. 3 Weight losses of alloy samples as functions of exposure time

Figure 4 shows the weight losses, on a percentage basis, of the three alloys where all the sample measurements were combined and represented as an average. Results are consistent with those shown in Fig. 3.

Fig. 4 Percentage weight losses of alloy samples as a function of exposure time

Table 2 shows the weight loss rates normalized with the sample surface area. Two features can be seen from Table 2: (a) the weight loss rates decrease for each alloy with the exposure time and (b) Haynes 230 and Inconel 625 appear to be better performers than SS 304. Based on the weight losses, the corrosion rates for SS 304, Inconel 625, and Haynes 230 were calculated as $r = \Delta W/(\rho A t)$ (where r is the corrosion rate, ΔW is the weight loss, ρ is the density, A is the total exposed area, and t is the exposure time). The calculated results are shown in Table 3. It should be pointed out that estimating corrosion rates based on weight loss measurements could give inaccurate results and hence absolute corrosion rates were calculated only to identify general trends in the corrosion process as a function of the exposure time.

Table 2 Average weight losses normalized with surface area and exposure time

Table 3 Corrosion rates based on average weight losses

In addition to weight monitoring, the diameter reductions of the samples were also recorded. The diameter reductions were not quite as representative of corrosion as the weight losses due to the fact that corrosion did not occur uniformly along the sample surface. Figure 5 shows the diameter reductions of the various samples as a function of the corrosion exposure time. In general, the diameter reductions follow the weight loss measurements, except for the 1000-h tests of Inconel 625 and Haynes 230.

Fig. 5 Percentage diameter reductions of alloy samples as a function of exposure time

As can be seen from Table 3 that the corrosion rates reduce with the exposure time. To further quantitatively illustrate this trend, the loss of the thickness is fitted as a power-law function of the exposure time: $D = kt^n$ (where D is the loss of the thickness and k and n are regression

parameters). The measurement results fit the equation well; and the regression parameters for SS 304, Inconel 625, and Haynes 230 are listed in Table 3. As shown in Table 3, the n values for three metal alloys are all less than 1, showing the corrosion rates decreasing with the exposure time.

5.2 Corrosion Rate Measurements Based on Corrosion Depths

To estimate corrosion depths, scanning electron microscopy (SEM) and energy dispersive x-ray analysis (EDS) tools were employed. Figures 6, 7, and 8 show typical SEM micrographs of corrosion on the sample surfaces of SS 304, Inconel 625, and Haynes 230 alloys, respectively, for various exposure time intervals.

Fig. 6 SEM images of corrosion progression in SS 304

Fig. 7 SEM images of corrosion progression in Inconel 625

Fig. 8 SEM images of corrosion progression in Haynes 230

It is interesting to see the differences in the corrosion morphology for the three alloys. For SS 304 samples shown in Fig. 6, corrosion at the surface was accompanied with cracks that extended inwards. At the 1000-h exposure time shown in Fig. 6d, there was also segregation of chromium along the grain boundaries as later confirmed with EDS.

For Inconel 625 samples and Haynes 230 samples shown in Figs. 7 and 8, respectively, the corrosion "affected zone" was well defined at the surface and accompanied with porosity which eventually linked up, as shown in Fig. 8c, resulting in mass removal. Furthermore, for all these alloys, after the 1000-h exposure time, the segregation of chromium was observed along the grain boundaries and at the sample surfaces.

For each of the samples evaluated, EDS was conducted to profile the elemental distributions near the surface and along the corrosion depth. These analyses were conducted for all the exposure time intervals for each of the alloys. However, for brevity, only images for the 1000-h exposure time are presented in Figs. 9, 10, and 11 for the three alloys.

Fig. 9 EDS elemental distribution maps on SS 304 corrosion sample post 1000-h exposure

Fig. 10 EDS elemental distribution maps on Inconel 625 corrosion sample post 1000-h exposure

Fig. 11 EDS elemental distribution maps on Haynes 230 corrosion sample post 1000-h exposure

Corrosion depth measurements at various exposure time intervals from samples of the three metal alloys are plotted in Fig. 12. For each sample, 20-30 measurements of corrosion depths around the sample circumference were made and reported in the plots. It should be noted that these measurements were from one of the flat ends of the sample. As shown in the plots, the corrosion depths are quite constant over the four exposure time intervals.

Fig. 12 Corrosion depth measurements for metal alloy samples

Additionally, the corrosion depths based on chromium segregation were also measured to illustrate the chromium segregation range change with the exposure time. These measurements were only made for the high-chromium alloys, Inconel 625 and Haynes 230, because chromium segregation was readily visible in these alloys. The results are plotted in Fig. 13 for the same samples as those in Figs. 12b and c. As expected, the corrosion depths based on chromium segregation were somewhat larger than those shown in Figs. 18b and c. For Haynes 230, this depth did not change significantly with the exposure time. This observation could be indicative of the oxidation of chromium at the surface being diminished, and consequently, diffusion or segregation of chromium was limited. For Inconel 625, however, the depth increased with the exposure time suggesting chromium diffusion was ongoing. This difference could be dependent on a variety of factors including grain size, alloy composition, etc. Analysis of additional samples will need to be made to arrive at a firm conclusion.

Fig. 13 Chromium segregation depth measurements for Inconel 625 and Haynes 230

6. Conclusions

In this study, the effects of $MgCl_2$ on the corrosion of SS 304, Inconel 625, and Haynes 230 alloys were investigated through embedded metal samples in a graphite foam/$MgCl_2$ medium heated to, and kept at, 750 °C for 100 h, 200 h, 500 h, and 1000 h. Experimental testing was conducted under a controlled environment after a moisture/oxygen removal process.

The corrosion rates were determined for the tested alloys by using (a) weight and dimension changes with the exposure time and (b) corrosion zone/depth changes with the exposure time using microscopy. The results showed that (a) the weight loss rates decreased for each alloy with the exposure time and (b) Haynes 230 and Inconel 625 appeared to be better performers than SS 304.

Additionally, the depths where chromium was segregated were also measured as functions of the exposure time for the high-chromium alloys: Inconel 625 and Haynes 230. As expected, the chromium segregation depths were somewhat larger than the corrosion depths. Furthermore, the depth did not change significantly with the exposure time for Haynes 230 while it increased with the exposure time for Inconel 625.

Acknowledgments

This work was sponsored by the Solar Energy Technologies Program of the U.S. Department of Energy under contract number DE-AC02-06CH11357 at Argonne National Laboratory, managed by UChicago Argonne LLC. Discussions with Dr. Levi Irwin on various aspects of this work are much appreciated.

References

1. W.B. Stine and R.B. Diver, Compendium of Solar Dish/Stirling Technology, Sandia National Laboratories: Albuquerque, NM, USA, 1994.
2. A. Gil, M. Medrano, I. Martorell, A. Lázaro, P. Dolado, B. Zalba, and L.F. Cabeza, State of the Art on High Temperature Thermal Energy Storage for Power Generation, Part 1—Concepts, Materials and Modellization, *Renew. Sustain. Energy Rev.*, 2010, **14**, p 31–55

3. M. Medrano, A. Gil, I. Martorell, X. Potau, and L.F. Cabeza, State of the Art on High-Temperature Thermal Energy Storage for Power Generation, Part 2-Case Studies, *Renew. Sustain. Energy Rev.*, 2010, **14**, p 56–72
4. J.I. Burgaleta, S. Arias, and D. Ramirez, Gemasolar, the First Tower Thermosolar Commercial Plant with Molten Salt Storage, in *SolarPACES2011*, SolarPACES, Granada, Spain, 2011, p 20–23
5. S. Kuravi, J. Trahan, D.Y. Goswami, M.M. Rahman, and E.K. Stefanakos, 2013. Thermal Energy Storage Technologies and Systems for Concentrating Solar Power Plants, *Progress in Energy and Combustion Science*, 2013, **39**, p 285–319
6. S. Qiu, L. Solomon, and M. Fang, Study of Material Compatibility for a Thermal Energy Storage System with Phase Change Material, *Energies*, 2018, **11** (3), 572. https://doi.org/10.3390/en11030572
7. S. Jegadheeswaran, S.D. Pohekar, and T. Kousksou, Exergy Based Performance Evaluation of Latent Heat Thermal Storage System: A Review, *Renew. Sustain. Energy Rev.*, 2010, **14**, p 2580–2595
8. J. Stekli, Thermal Energy Storage and the United States Department of Energy's SunShot Initiative, in *SolarPACES2011*, SolarPACES, Granada, Spain, 2011
9. M. Mehos, C. Turchi, J. Vidal, M. Wagner, Z. Ma, C. Ho, W. Kolb, C. Andraka, A. Kruizenga, Concentrating Solar Power Gen3 Demonstration Roadmap, National Renewable Energy Laboratory Technical Report NREL/TP-5500-67464, 2017
10. W. Ding, A. Bonk, and T. Bauer, Corrosion Behavior of Metallic Alloys in Molten Chloride Salts for Thermal Energy Storage in Concentrated Solar Power Plants: A review, *Front. Chem. Sci. Eng.*, 2018, **12**(3), p 564–576. https://doi.org/10.1007/s11705-018-1720-0
11. B. Zalba, J.M. Marin, L.F. Cabeza, and H. Mehling, Review on Thermal Energy Storage with Phase Change: Materials, Heat Transfer Analysis and Applications, *Applied Thermal Engineering*, 2003, **23**, p 251–283
12. M. Lacroix, Study of the Heat Transfer Behavior of a Latent Heat Thermal Energy Storage Unit with a Finned Tube, *Int. J. Heat Mass Transfer*, 1993, **36**, p 2083–2092
13. R. Velraj, R.V. Seeniraj, B. Hafner, C. Faber, and K. Schwarzer, Experimental Analysis and Numerical Modelling of Inward Solidification on a Finned Vertical Tube for a Latent Heat Storage Unit, *Solar Energy*, 1997, **60**, p 281–290
14. A. Miliozzi, R. Liberatore, T. Crescenzi, and E. Veca, Experimental Analysis of Heat Transfer in Passive Latent Heat Thermal Energy Storage Systems for CSP Plants, *Energy Procedia*, 2015, **82**, p 730–736
15. C.W. Robak, T.L. Bergman, and A. Faghri, Enhancement of Latent Heat Energy Storage Using Embedded Heat Pipes, *Int. J. Heat Mass Transfer*, 2011, **54**, p 3476–3484
16. H. Shabgard, T.L. Bergman, N. Sharifi, A. Faghri, High Temperature Latent Heat Thermal Energy Storage Using Heat Pipes, *Int. J. Heat Mass Transfer*, 2010, **53**, p 2979–2988
17. R. Siegel, Solidification of Low Conductivity Material Containing Dispersed High Conductivity Particles, *Int. J. Heat Mass Transfer*, 1977, **20**, p 1087–1089
18. S.T. Hong and D.R. Herling, Open-Cell Aluminum Foams Filled with Phase Change Materials as Compact Heat Sinks, *Scripta Materialia*, 2006, **55**, p 887–890
19. S. Krishnan, J.Y. Murthy, and S.V. Garimella, A Two-Temperature Model for Solid-Liquid Phase Change in Metal Foams, *ASME Transactions Journal of Heat Transfer*, 2005, **127**, p 995–1004
20. A. Siahpush, J. O'Brien, and J. Crepeau, Phase Change Heat Transfer Enhancement Using Copper Porous Foam, *ASME Transactions Journal of Heat Transfer*, 2008, **130**, paper number 082301
21. C.Y. Zhao and Z.G. Wu, Heat Transfer Enhancement of High Temperature Thermal Energy Storage Using Metal Foams and Expanded Graphite, *Solar Energy Materials and Solar Cells*, 2011, **95**, p 636–643
22. T. Kim, D.M. France, W. Yu, W. Zhao, and D. Singh, Heat Transfer Analysis of a Latent Heat Thermal Energy Storage System Using Graphite Foam for Concentrated Solar Power, *Solar Energy*, 2014, **103**, p 438–447
23. W. Zhao, D.M. France, W. Yu, T. Kim, and D. Singh, Phase Change Material with Graphite Foam for Applications in High-Temperature Latent Heat Storage Systems of Concentrated Solar Power Plants, *Renewable Energy*, 2014, **69**, p 134–146
24. D. Singh, W. Zhao, W. Yu, D.M. France, and T. Kim, Analysis of a Graphite Foam-NaCl Latent Heat Storage System for Supercritical CO2 Power Cycles for Concentrated Solar Power, *Solar Energy*, 2015, **118**, p 232–242
25. D. Singh, T. Kim, W. Zhao, W. Yu, and D.M. France, Development of Graphite Foam Infiltrated with $MgCl_2$ for a Latent Heat Based Thermal Energy Storage (LHTES) System, *Renewable Energy*, 2016, **94**, p 660–667
26. D. Singh, W. Yu, W. Zhao, T. Kim, D.M. France, and R.K. Smith, Development and Prototype Testing of $MgCl_2$/Graphite Foam Latent Heat Thermal Energy Storage System, *Solar Energy*, 2018, **159**, p 270–282
27. D. Singh, W. Yu, W. Zhao, T. Kim, D.M. France, and R. K. Smith, High-Efficiency Thermal Energy Storage System for Concentrated Solar Power, Argonne National Laboratory Report ANL/ESD-17/10, 2017

28. K. Nithyanandam and R. Pitchumani, Design and Analysis of Metal Foam Enhanced Latent Thermal Energy Storage with Embedded Heat Pipes for Concentrating Solar Power Plants, in *Proceedings of ASME 2013 7th International Conference on Energy Sustainability and 11th Fuel Cell Science*, 2013
29. I.N. Ozeryanaya, Corrosion of Metals by Molten Salts in Heat Treatment Processes, *Metal Science and Heat Treatment*, 1985, **27**, p 184–188
30. P. Sabharwall, M. Ebner, M. Sohal, P. Sharpe, M. Anderson, K. Sridharan, J. Ambrosek, L. Olson, and P. Brooks, Molten Salts for High Temperature Reactors: University of Wisconsin Molten Salt Corrosion and Flow Loop Experiments—Issues Identified and Path Forward, Idaho National Laboratory Report INL/EXT-10-18090, 2010
31. A.M. Kruizenga, Corrosion Mechanisms in Chloride and Carbonate Salts, Sandia National Laboratory Report SAND2012-7594, 2012
32. M. Zhu, H. Ma, M. Wang, Z. Wang, and A. Sharif, Effects of Cations on Corrosion of Inconel 625 in Molten Chloride Salts, *High Temperature Materials and Processes*, 2016, **35** (4), p 337–345
33. AK Steel Corporation, 304/304L Stainless Steel, https://www.aksteel.com/sites/default/files/2018-01/304304L201706_1.pdf
34. Special Metals Corporation, Inconel Alloy 625, http://www.specialmetals.com/assets/smc/documents/alloys/inconel/inconel-alloy-625.pdf
35. Haynes International, Haynes 230 Alloy, http://haynesintl.com/docs/default-source/pdfs/new-alloy-brochures/high-temperature-alloys/brochures/230-brochure.pdf
36. Q. Huang, G. Lu, J. Wang, and J. Yu, Thermal Decomposition Mechanisms of $MgCl_2$-$6H_2O$ and $MgCl_2$-H_2O, *Journal of Analytical and Applied Pyrolysis*, 2011, **91**, p 159-164
37 M. Romanoff, Underground Corrosion, National Bureau of Standard Circular 579, 1957

Table 1 Chemical composition of three metal alloys (mass %)

	B	C	N	Al	Si	P	S	Ti	Cr	Mn	Fe	Co	Ni	Nb	Mo	La	W
SS 304		0.08 max.	0.1 max.		0.75 max.	0.045 max.	0.03 max.		18-20	2 max.	Balance		8-12				
Inconel 625		0.1 max.		0.4 max.	0.5 max.	0.015 max.	0.015 max.	0.4 max.	20-23	0.5 max.	5 max.	1.0 max.	58 min.	3.15-4.15 (Nb+Ta)	8-10		
Haynes 230	0.015 max.	0.1		0.3	0.4			0.1 max.	22	0.5	3 max.	5 max.	57	0.5 max.	2	0.02	14

Table 2 Average weight losses normalized with surface area and exposure time

	SS 304 (mg/cm^2h)	Inconel 625 (mg/cm^2h)	Haynes 230 (mg/cm^2h)
100 h	0.0513 ± 0.007	0.0149 ± 0.004	0.0118 ± 0.007
200 h	0.0345 ± 0.003	0.0064 ± 0.002	0.0054 ± 0.002
500 h	0.0144 ± 0.001	0.0032 ± 0.001	0.0025 ± 0.0004
1000 h	0.0085 ± 0.001	0.0008 ± 0.002	0.0008 ± 0.0002

Table 3 Corrosion rates based on average weight losses

	SS 304 (μm/year)	Inconel 625 (μm/year)	Haynes 230 (μm/year)
100 h	562.44	155.13	114.92
200 h	377.29	66.80	53.03
500 h	157.76	33.71	24.28
1000 h	93.57	8.55	7.98
	SS 304	**Inconel 625**	**Haynes 230**
k*	2.7403	1.2407	1.0487
n*	0.1975	0.0621	0.0401

* For Inconel 625 and Haynes 230, *k* and *n* are based on the measurements for 100 h, 200 h, and 500 h only.

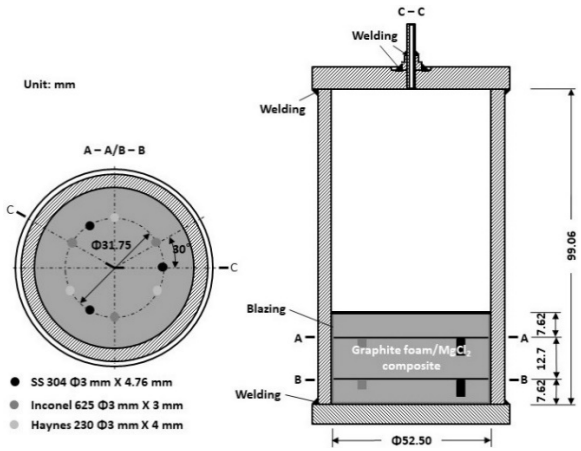

(a) Schematic of test modules

(b) Machined graphite foam disks

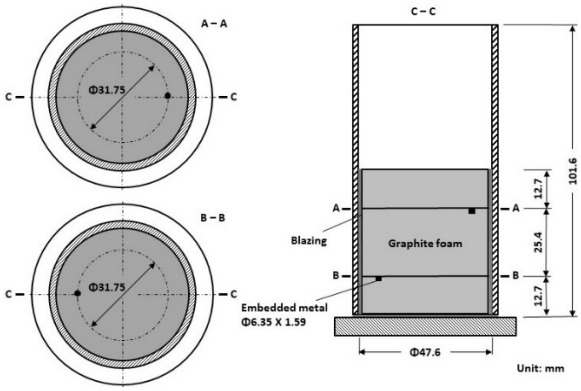

(c) Infiltration test containers

(d) Cut-open views of infiltrated container

(e) Completed corrosion test modules

(f) Capped corrosion test modules

(g) Embedded alloy samples

Fig. 1 Corrosion test modules and alloy test samples

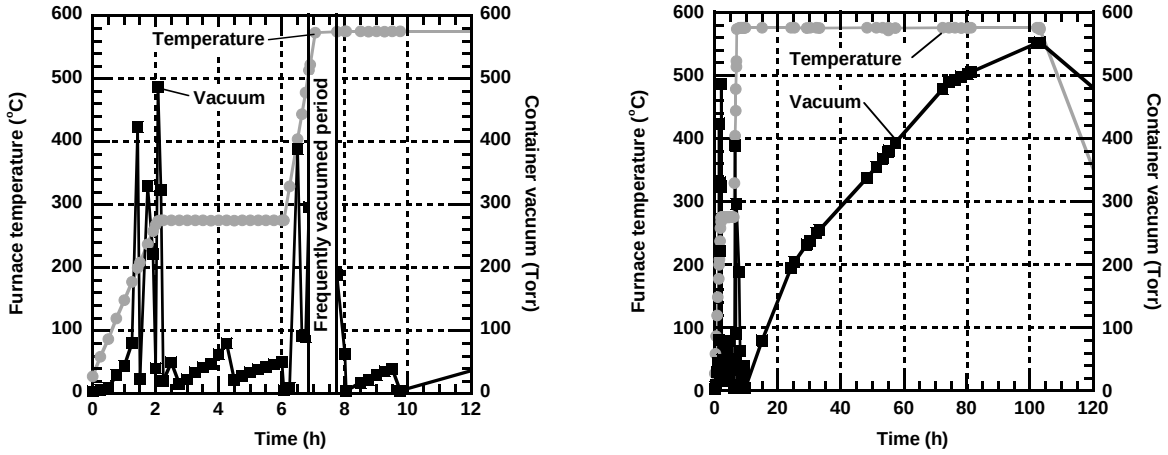

Fig. 2 Temperature and pressure profiles during moisture removal process

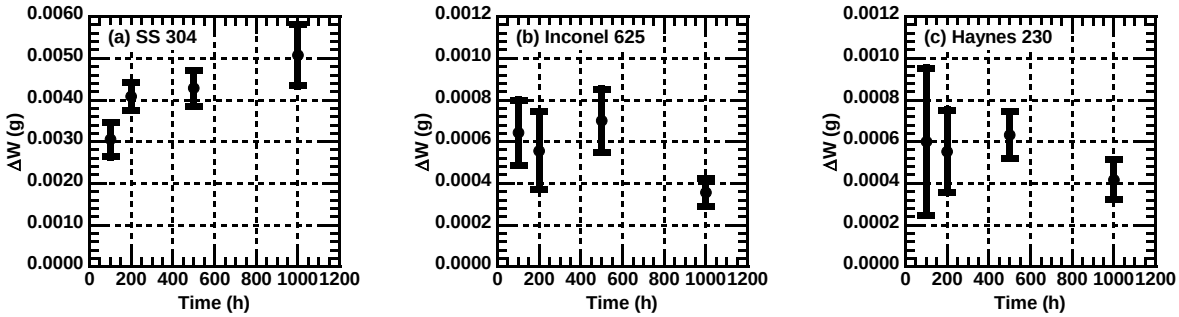

Fig. 3 Weight losses of alloy samples as functions of exposure time

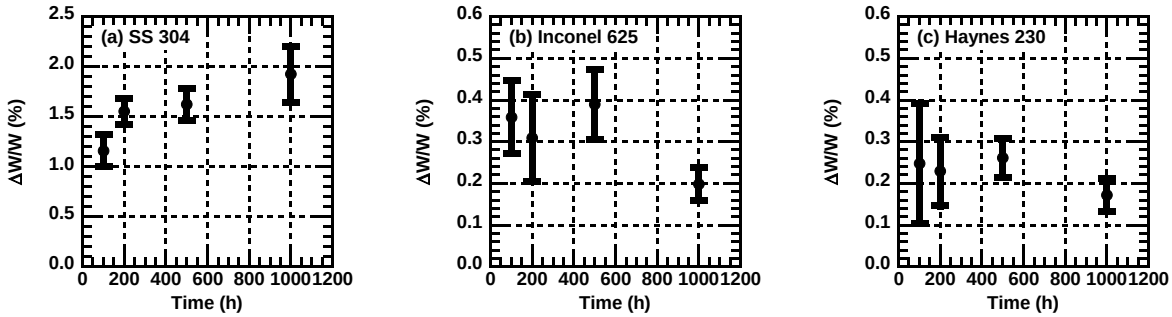

Fig. 4 Percentage weight losses of alloy samples as a function of exposure time

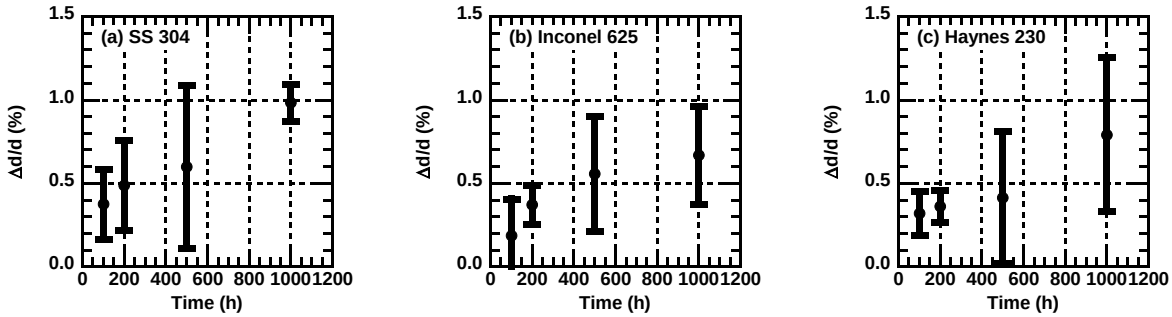

Fig. 5 Percentage diameter reductions of alloy samples as a function of exposure time

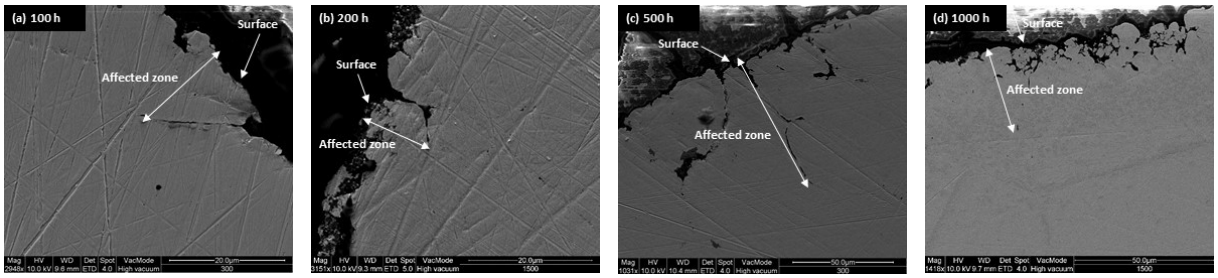

Fig. 6 SEM images of corrosion progression in SS 304

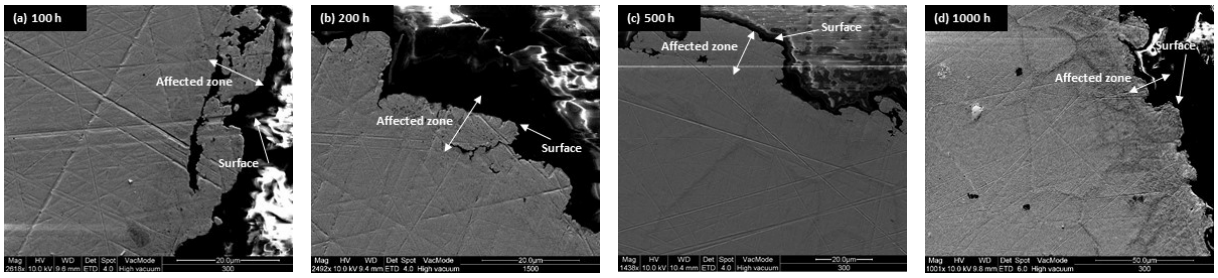

Fig. 7 SEM images of corrosion progression in Inconel 625

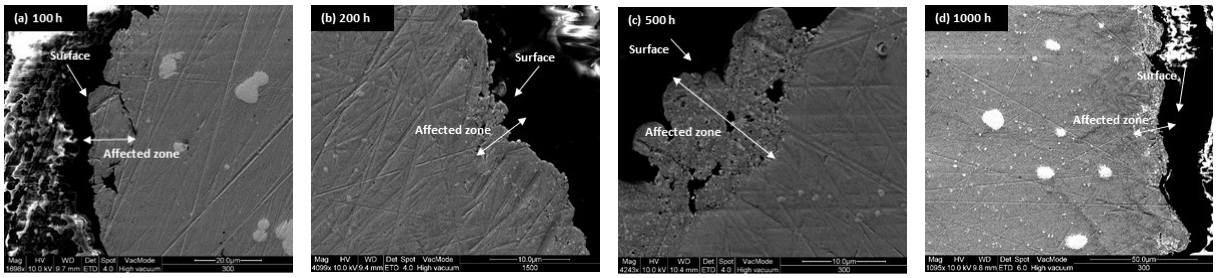

Fig. 8 SEM images of corrosion progression in Haynes 230

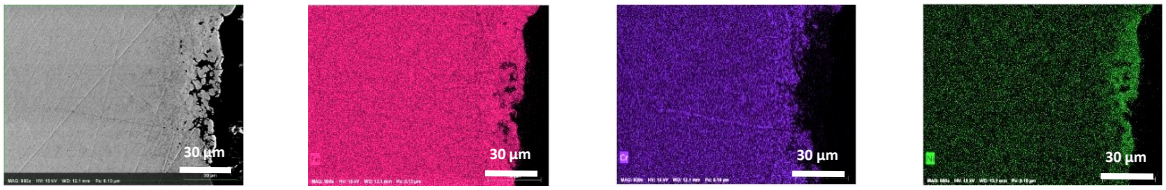

(a) **(b)** Fe **(c)** Cr **(d)** Ni

Fig. 9 EDS elemental distribution maps on SS 304 corrosion sample post 1000-h exposure

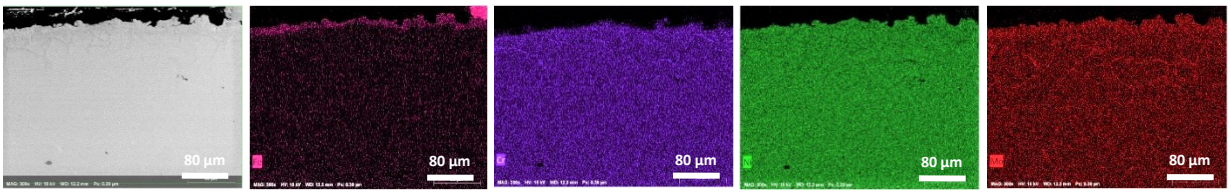

(a) **(b)** Fe **(c)** Cr **(d)** Ni **(e)** Mo

Fig. 10 EDS elemental distribution maps on Inconel 625 corrosion sample post 1000-h exposure

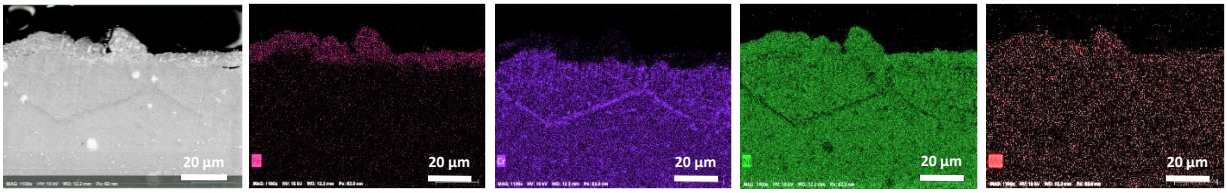

(a) **(b)** Fe **(c)** Cr **(d)** Ni **(e)** Mo

Fig. 11 EDS elemental distribution maps on Haynes 230 corrosion sample post 1000-h exposure

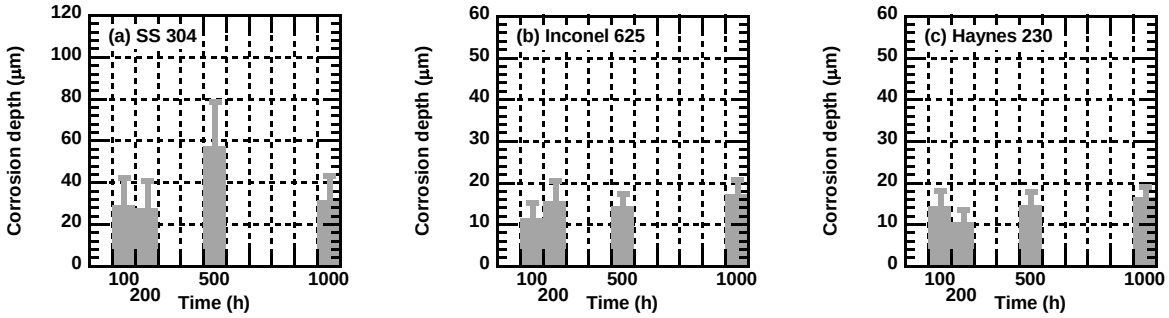

Fig. 12 Corrosion depth measurements for metal alloy samples

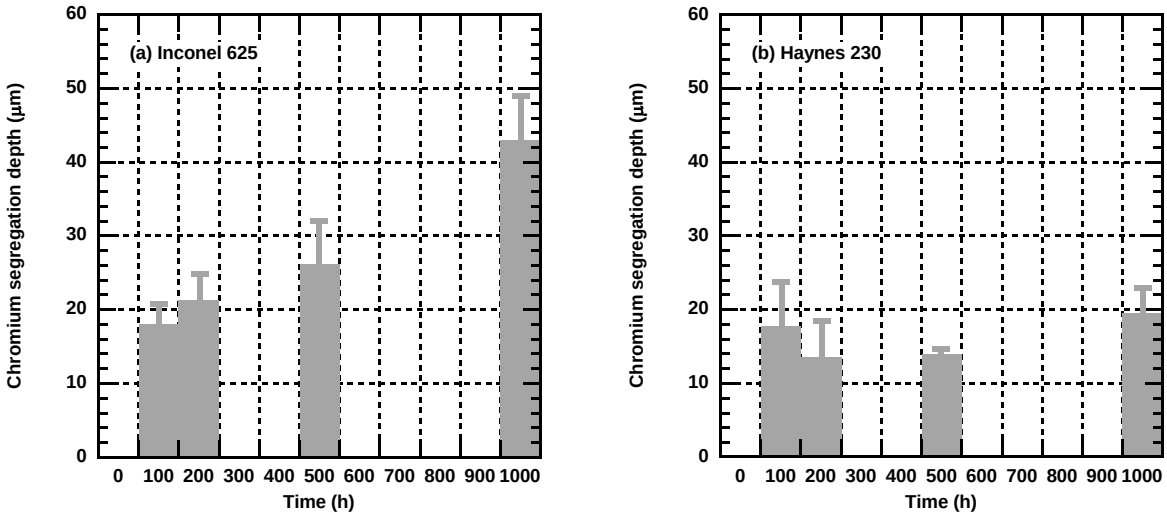

Fig. 13 Chromium segregation depth measurements for Inconel 625 and Haynes 230